1-27-2023

A new mechanism for glymphatic flow of interstitial fluid in branched perivascular spaces of the brain

Charles F. Babbs
Purdue University, babbs@purdue.edu

A new mechanism for glymphatic flow of interstitial fluid in branched perivascular spaces of the brain

Charles F. Babbs, MD, PhD, Weldon School of Biomedical Engineering,
Purdue University, January 27, 2023

Abstract

Objective. To explore the biophysics of interstitial tissue fluid flow in the brain, based upon the anatomy and mechanics of the perivascular spaces, in order to better understand how glymphatic flow happens.

Methods. The dynamics of fluid flow at cardiac frequencies are investigated in rapidly computable, branched, geometric models of brain tissue at multiple scales. The models are supplied by intermingled trees of penetrating arteries and veins. They include pulsatile changes in intracranial pressure and intravascular pressure, elastic expansion of brain tissue, and nonlinear changes in resistance to flow of cerebrospinal fluid along the axis of the Virchow-Robin space. Resulting changes in periarterial and perivenous pressures and the resulting bulk flow of interstitial fluid from arteriolar to venular perivascular spaces are calculated on a laptop computer.

Results. Under typical physiological conditions a time averaged positive pressure of ~ 0.5 mmHg develops between the smaller, distal periarteriolar and perivenous branches. Based on tissue geometry and hydraulic resistance, the resulting flow is sufficient to refresh the interstitial fluid once every 1 to 10 hours. The effect is degraded by increasing radial widths of the perivascular spaces. The calculated average glymphatic flow through the whole brain is similar to the measured production of new cerebrospinal fluid by the arachnoid villi.

Conclusions. When the branching structure of perivascular trees is properly considered, their classical anatomy has surprising emergent properties. Biologically meaningful amounts of advective flow can happen between smaller, distal branches of periarteriolar and perivenous spaces.

Key words. advection, Alzheimer's disease, amyloid, biophysics, blood brain barrier, bulk flow, cerebrospinal fluid, circulation, extracellular, hydraulic, intracranial pressure, perivascular pumping, permeability, pia mater, pulsation, subarachnoid space, Virchow-Robin space, waste.

Introduction

All tissues in the body have a second fluid and solute transport system in addition to the cardiovascular system. In the periphery, a steady influx of plasma ultrafiltrate through capillaries drives interstitial fluid into tissues, most of which re-enters capillaries at their venular ends. This process by which water and small to medium sized molecules circulate through gaps between capillary endothelial cells is known as Starling's equilibrium of the capillary. Residual tissue fluid that is not returned to the blood stream by the Starling mechanism is drained by lymphatic vessels.

In the central nervous system, however, the blood brain barrier eliminates the usual Starling mechanism. There are no lymphatic channels or lymph nodes. Instead, interstitial fluid is refreshed and waste products removed by pulsatile, net unidirectional "glymphatic" fluid flow, a term coined by Iliff et al.[1], who found that tracers injected into cerebrospinal fluid (CSF) were swept into Virchow-Robin spaces surrounding penetrating arteries, entered the brain's extracellular space, and accumulated around veins. Tracer studies reveal that there must be a continuous pathway through periarteriolar spaces and brain tissue into perivenous spaces, providing a low-resistance route for CSF flow[2]. Among such tracers is amyloid beta, a toxic protein that accumulates in Alzheimer's disease[1-3].

Because of the likely connections of glymphatic flow to the pathogenesis of Alzheimer's disease, stroke, vascular dementia, and other neurodegenerative disorders[3], the study of glymphatic fluid flow as attracted a large community of investigators, leading to thousands of research publications, which have been well reviewed[4-11]. In principle, the observed net flow of interstitial fluid in the brain should be driven by a small, net-positive pressure gradient. However, defining the exact mechanism responsible for such a gradient remains an open problem[4,11-15]. Especially lacking are mechanisms and models including arterial and venous vascular trees with branches of realistic length and diameter, and including brain tissue surrounding perivascular spaces that is soft enough to be deformed significantly when artery walls pulsate[4,14]. The present paper takes a fresh, first-principles approach to this open problem, resulting in a new, computationally simple, dynamic model of glymphatic fluid flow. The model is based upon the classical anatomy of the perivascular or Virchow-Robin space, which may constitute an effective pulsatile pump that has been hiding in plain sight.

Figure 1, drawn artfully by Laurence Weed in 1923[8] illustrates the unique anatomy of blood vessels in the subarachnoid space, including penetrating branches diving into the cerebral cortex. The branching vascular trees and the channels into which they penetrate are covered by thin layers of pia mater, creating a cuff or sleeve-like perivascular space that is unique to the central nervous system. The perivascular space continues downward into the brain for many orders of arterial or venous branches. The diameters of the perivascular spaces are roughly twice those of the companion blood vessels at each order of branching (Figure 1) with veins having roughly twice the diameters, much thinner smooth muscle walls, and much greater compliances than their companion arteries.

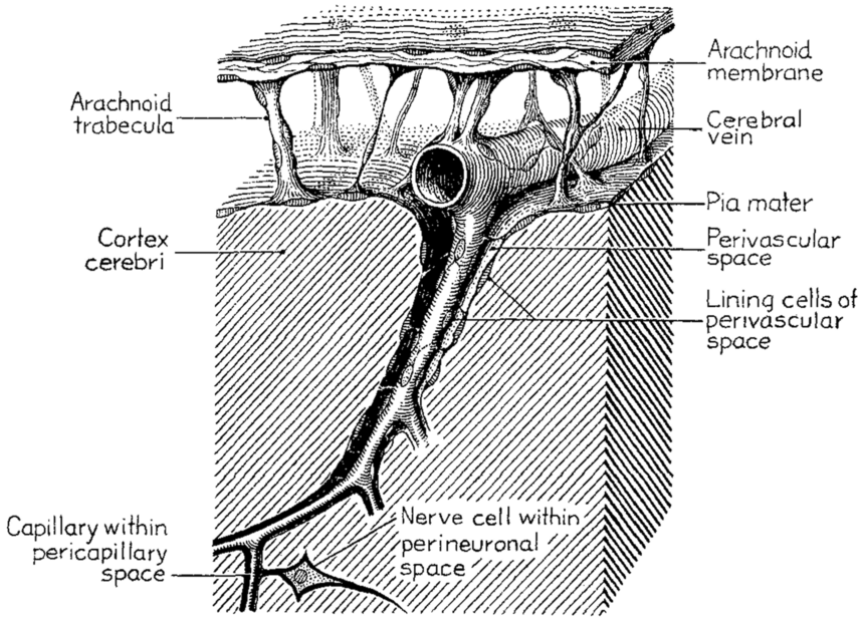

Figure 1: Relevant anatomy, as drawn by Lawrence Weed in 1923 [8].

A conceivable perivascular pump mechanism

The breakthrough insight inspiring the present work is that this well-known and simple anatomy may provide a hidden and unappreciated mechanism for pumping of cerebrospinal fluid from the periarterial to the perivenous spaces. After some preliminary work with early models, a working hypothesis emerged. Pressure in the subarachnoid space, also known as intracranial pressure (ICP) remains nearly constant at ~ 10-20 mmHg, but does have pulsatile fluctuations in association with the heartbeat. These changes are clearly shown on clinical recordings, such as that sketched in Figure 2.

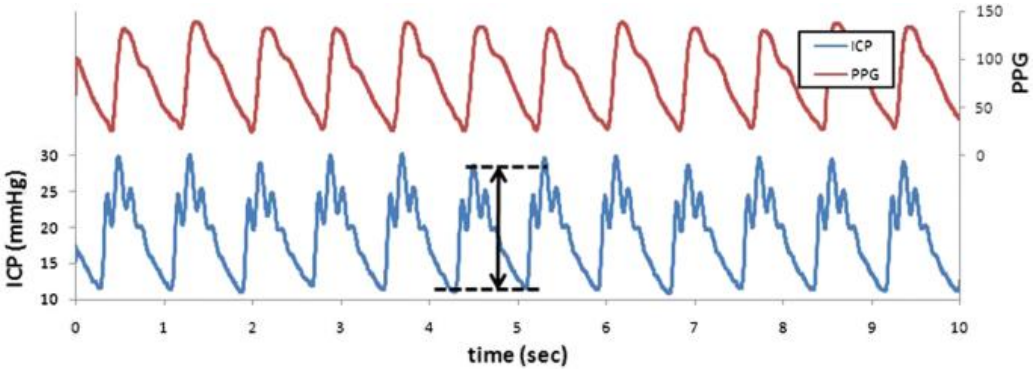

Figure 2: Time domain waveforms of peripheral arterial pulse and intracranial pressure from Evensen[16]. ICP indicates intracranial pressure. PPG indicates photoplethysmogram.

The waveforms and timing of the ICP pulses suggest that they likely arise from expansion of arteries in the subarachnoid space. For the purpose of understanding the perivascular pump mechanism, it is the changes in pressure with respect to the mean value of ICP, denoted ΔP, that are of consequence for cerebrospinal fluid flow. A value of $\Delta P = 0$ corresponds to mean ICP. When ICP increases during systolic expansion of larger arteries on the brain surface, subarachnoid pressure will increase and fluid will flow into both periarteriolar and perivenous perivascular spaces from the subarachnoid space (Figure 3). Simultaneously there will be elastic expansion of soft surrounding brain.

On the venous side there will be volume compensation caused by partial collapse of the thin-walled vein with low internal pressure. However, on the arterial side there will be pulsatile expansion of the artery, further increasing periarterial space pressure, and simultaneously narrowing the perivascular space, increasing its resistance to outflow between heartbeats. In turn, excess fluid and pressure could accumulate in the periarterial space compared to the perivenous space. The resulting time averaged differences in periarterial and perivenous pressure could drive glymphatic fluid flow.

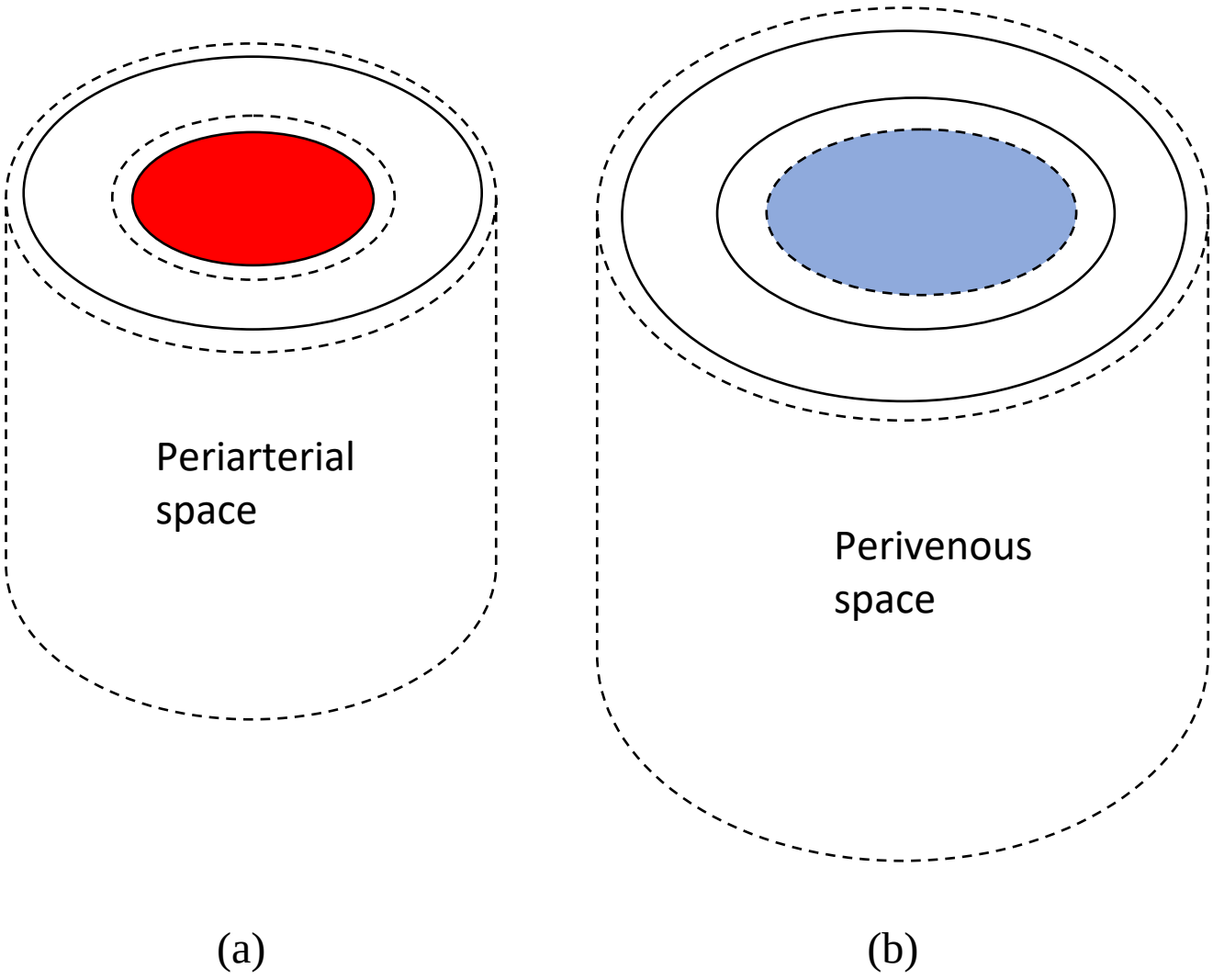

***Figure 3:** Motions of walls of the shaded perivascular spaces. Solid lines indicate end-diastole; dashed lines indicate end-systole. (a) In the periarterial space brain tissue forming the outer wall moves radially outward, and the artery forming the inner wall also moves radially outward. (b) In the perivenous space brain tissue forming the outer wall moves radially outward, however the vein forming the inner wall moves radially inward, further relieving pressure. Opposite effects happen during diastole.*

On the arterial side, fluid in the perivascular space is squeezed by the expanding blood vessel, increasing pressure and also increasing resistance to outflow into the subarachnoid space. If outflow resistance from the periarteriolar space is high because of relative channel narrowing and nonlinear increases in resistance (and RC time constant), then there would be incomplete drainage of excess systolic pressure into the subarachnoid space before the next arterial pulse. On the venous side, fluid in the larger perivascular space is decompressed from brain side and also decompressed from the venous side, so average pressure and resistance remain less. These effects might lead to accumulation of net positive perivascular pressure on the arterial side compared to the venous side, owing to a fundamental asymmetry between peri-arteriolar spaces and peri-venous spaces.

Mathematical models are an excellent way to explore, test, and refine understanding of such mechanisms and to determine if they could cause sufficient pressure differences to drive biologically meaningful glymphatic fluid flow. This paper details the development and testing of such a model to determine if the perivascular spaces might, in fact, constitute an unappreciated pump for glymphatic flow.

Methods

Geometric model of brain tissue domains

Figure 4 shows a simplified model of the perivascular space surrounding a branched artery or vein in the cerebral cortex.

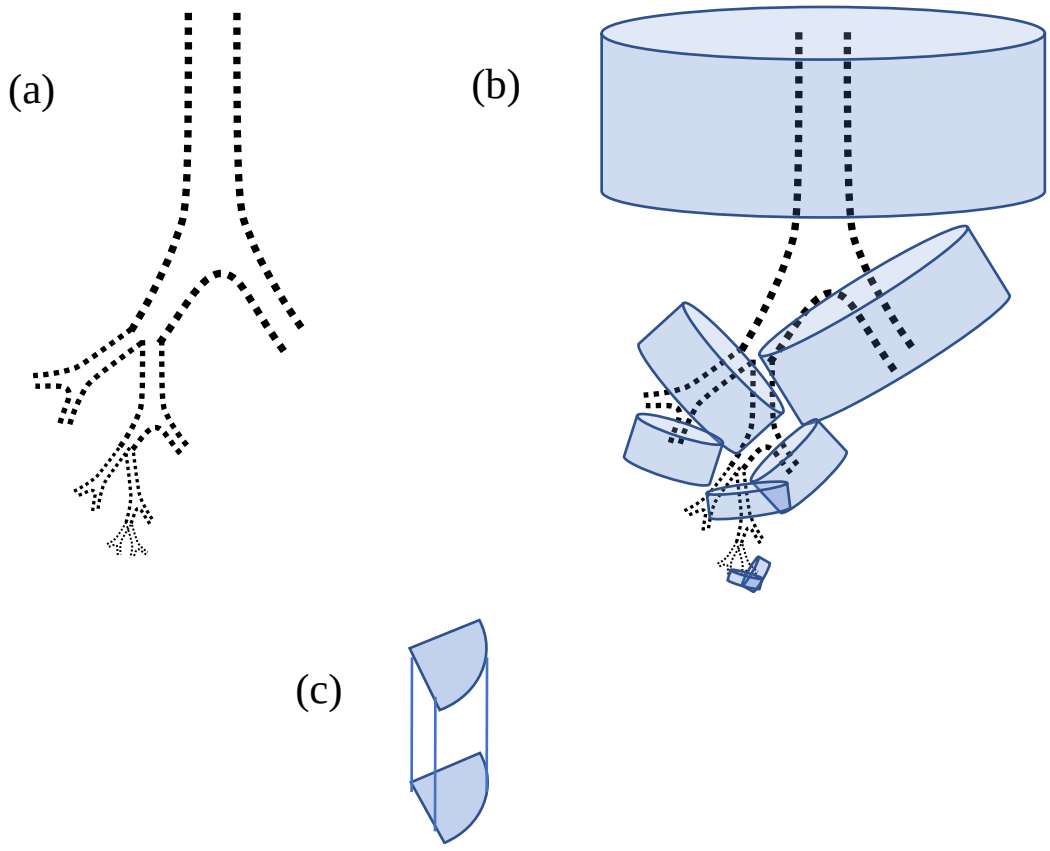

Figure 4: Branching tree of perivascular spaces, without (a) and with (b) representative cylindrical domains of surrounding brain tissue. A given brain cell may be part of more than one domain. For clarity, not all overlapping domains are shown. Trees of domains encompass nearly all brain tissue. Each full cylindrical domain can be divided into quarter cylinder sectors for convenience in pairing neighboring arterial and venous watersheds (c) , as suggested in Figure 5.

Here, for simplicity, each parent vessel gives rise to two and only two daughter vessels. The narrowing and shortening of the branching pattern is determined by a branching factor, α , such as 0.75, that describes the fractional reduction in linear dimensions, both radius and length, of blood vessels at each successive level. As shown in Appendix 1, a branching factor of the square root of one half (0.707) describes an idealized tree with equal cross-sectional area at each level, permitting equal volumetric flow with equal velocity. However, given classical Poiseuille resistance ($\sim 1/r^4$) , a branching factor of cube root of one half (0.794) describes a tree in which the tradeoff between increasing numbers of vessels and decreasing caliber of vessels at each level produces a constant, linear stepwise reduction in pressure at each level, as described experimentally[17-19] and in classical textbook physiology. Accordingly, for present purposes, a branching factor $\alpha = 0.75$ is used as a compromise value to describe an idealized cerebrovascular tree. Note that a given brain cell may be part of more than one domain. However, as will be seen subsequently, glymphatic fluid flow is greatest in the smallest domains at the highest level of branching.

Looking down on the surface of the cerebral cortex from above (Figure 5), one can imagine a honeycomb-like pattern of roughly cylindrical tissue domains packed together. These largest domains, surrounding the largest vessels penetrating the surface of the brain, represent first order branches of modeled arterial and venous vascular trees. As shown in Figures 5 and 6, by dividing each cylinder into four quarter cylinders it is possible to match back-to-back arterial and venous territories to represent a volume of tissue fed by a particular artery and drained by a particular companion vein at each level of branching. Conceptually, one can represent the glymphatic bulk flow as that occurring between overlapping peri-arterial and peri-venous domains of tissue at each level of branching, despite biological irregularities in the locations of arteries and veins.**

** Footnote: Interestingly, for an ideal checkerboard pattern with alternating dark squares representing tissue around arteries and alternating white squares representing tissue around veins, it is easy to demonstrate that a perfect tiling of diamond shaped spaces, half dark and half white, with points at the centers of each checkerboard square, perfectly fills the plane.

Figure 5(a) shows the present geometric model viewed from a patch of cortical surface. There are equal numbers of arteries and veins at multiple levels in a hexagonal lattice, similar to the approach of Jin et al.[20] and Schreder et al.[14]. To simplify subsequent mathematics using radial symmetry, the back-to-back overlapping of paired arterial and venous domains can be represented as overlapping arcs of quarter cylinders (Figure 5(b)).

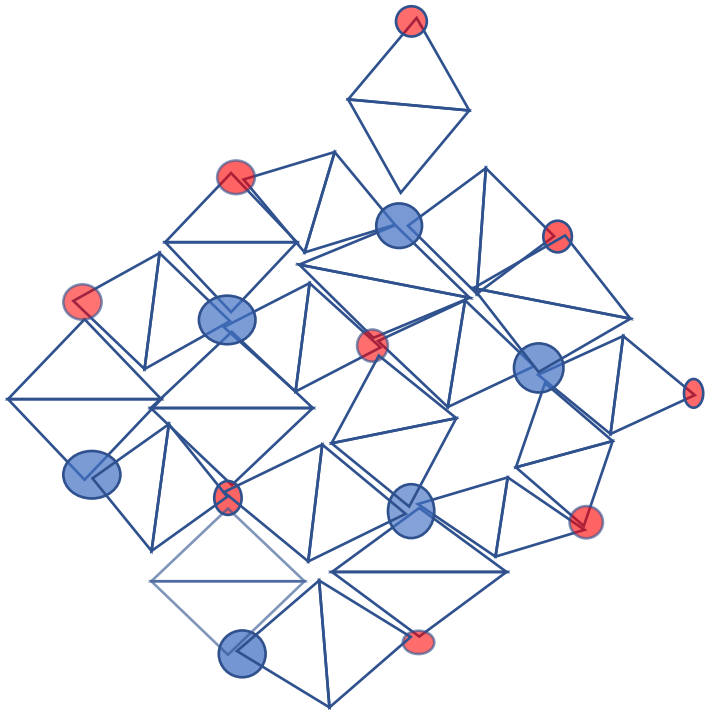

(a)

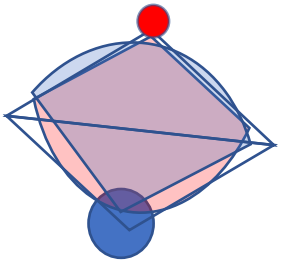

(b)

Figure 5. Quarter cylindrical tissue domains representing regions of local glymphatic flow between pairs of smaller arterial and larger venous perivascular spaces at a particular branching level. (a) composite arrangement (b) zones of overlapping arterial and venous vascular trees.

Correction for total volume of tissue domains

The tissue domain radii, $r_3(n)$, for each branching level, n , are jointly subject to the constraint that at the last branching level (e.g. $r_3(10)$) the total volume of the domains should equal the total volume of the one column of cortical tissue with radius $r_3(1)$ and length, D , representing the full thickness of cerebral cortex (Figure 6). This constraint ensures that all brain cells within a short distance of both a terminal arteriole and a terminal venule will be served by both an artery and a vein, and that the total volume of the model is conserved.

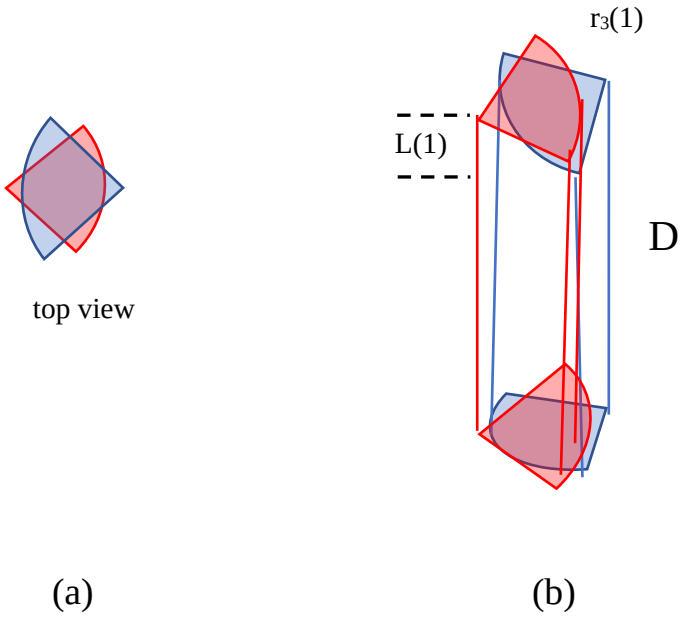

Figure 6: Paired, overlapping quadrants of coupled arterial and venous vascular trees (a) top view, (b) perspective view of the full cortical thickness.

This constraint means that the stepwise reduction in the outer radii of tissue domains, $r_3(n)$, at each branching level, n , may be different than the stepwise reduction in vascular lengths and radii, branching factor α . Let β represent the reduction factor for tissue domain radii $r_3(n)$ at each branch. Consider a vascular tree with a total of N+1 branching levels, including the first, with N generations of daughter branches. For volume conservation we must have

$$\pi r_3^2(1)D = 2^N \pi r_3^2(1)\beta^{2N} L(1)\alpha^N \,, \qquad (1)$$

where L(1) represents the length of the first, longest arterial or venous segments and $r_3(1)$ represents its radius . In turn,

$$\alpha\beta^2 = \left(\frac{1}{2^N} \cdot \frac{D}{L(1)}\right)^{\frac{1}{N}} = \frac{1}{2}\left(\frac{D}{L(1)}\right)^{\frac{1}{N}}, \quad (2)$$

and

$$\beta = \sqrt{\frac{1}{2\alpha}\left(\frac{D}{L(1)}\right)^{\frac{1}{N}}}, \quad (3)$$

For example, if $\alpha = 0.75$, as before, N = 9 generations of branches, and D/L(1) = 4.5 for the human cerebral cortex, then

$$\beta = \sqrt{\frac{1}{2(0.75)}(4.5)^{\frac{1}{9}}} = 0.888, \quad (4)$$

and $\frac{\beta}{\alpha} = \frac{0.888}{0.75} = 1.1784$. Geometrically, therefore, the vascular and perivascular radii r_1 and r_2 will be reduced by factor, α, at each branching level, but outer tissue domain radius r_3 will be reduced by a slightly larger factor, $\beta = 1.184\ \alpha$, at each branching level. After 9 successive orders of branching, the ratio of r_3/r_2, representing the relative thickness of the outer cylindrical shell of tissue, would be $\left(\frac{\beta}{\alpha}\right)^9 = 4.573$ This difference will increase the relative resistances of the smaller domains to bulk flow, as described by Darcy's law, and slow calculated glymphatic flow.

Discretized model

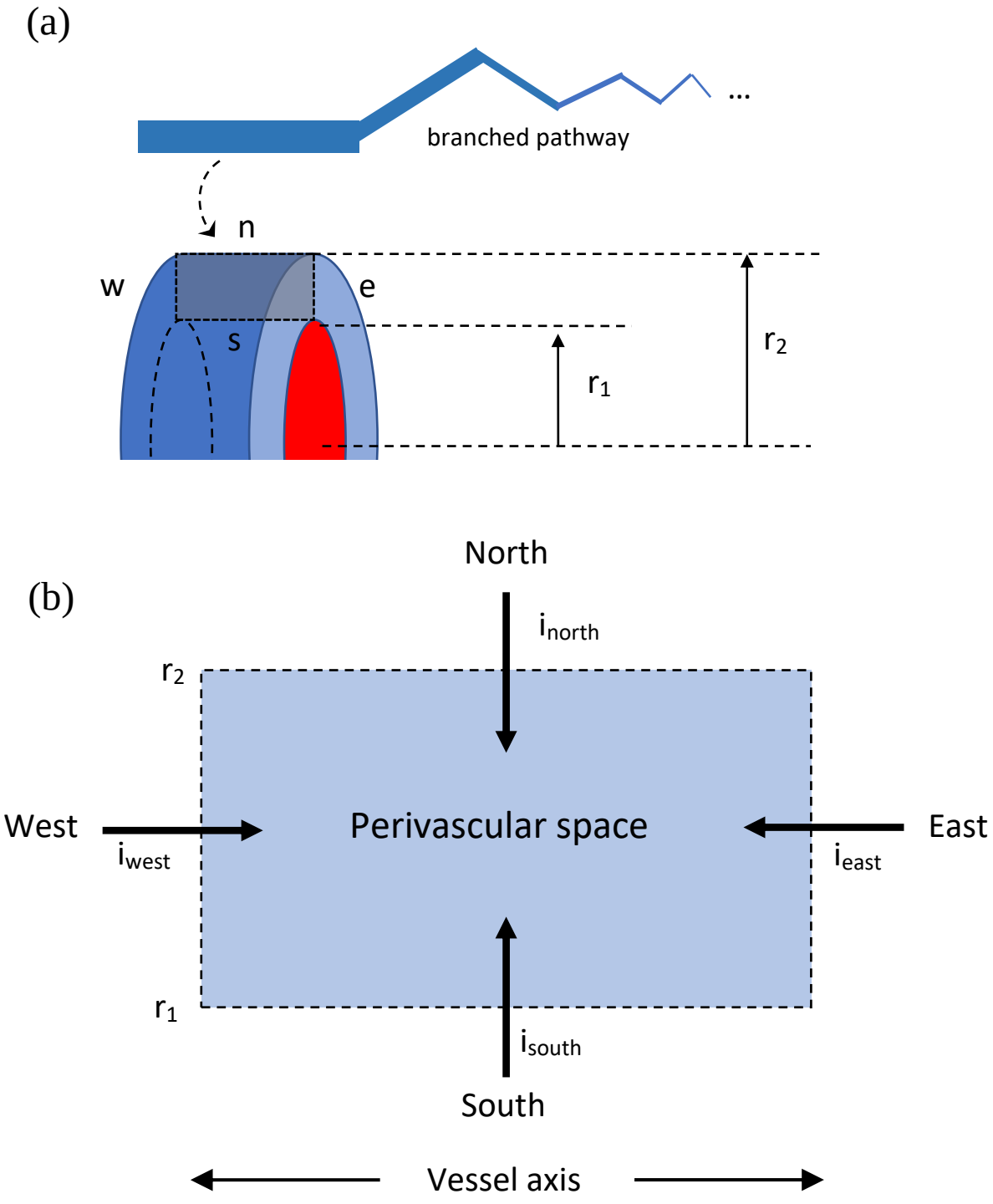

Figure 7. Sketches of one sector at one branching level of the perivascular space. North border represents surrounding brain. South border represents blood vessel wall. East-West axis is parallel to blood flow.

In Figure 7 the long axis of the perivascular space is horizontal and radial axis is vertical. Axial flow from right to left indicates inflow from the subarachnoid space, deeper into the brain. Flow from left to right indicates outflow into the subarachnoid space. The upper, "north" edge represents the pia covered brain surface. The "south" edge represents the pia covered vascular surface. The dimension in and out of the page is the "hoop" or circumferential dimension. These diagrams represent just one branch of a vascular tree. With successive branches the vascular dimensions become smaller according to the branching factor, α .

The axial length of the cylindrical domain is denoted L. Each domain surrounds a central vessel in a pattern similar to that of a microscopic liver lobule surrounding its central vein. Radius r_1 represents the radius of the artery or vein. Radius r_2 represents the radius of the extended Virchow-Robin space. Radius r_3 represents the outer boundary of the brain tissue domain, which in this geometric model approximates the separation between an artery and its companion vein in the cerebral cortex. Here $r_1 < r_2 << r_3$.

Changes in perivascular volumes and pressures

Consider first a brain penetrating artery surrounded by its perivascular cuff. Radial directions correspond to the north--south direction, and axial directions correspond to the east--west direction. CSF can flow along the east--west axis of the perivascular space from one discrete segment to another. These flows are denoted as i_{east} and i_{west} in Figure 7 , with signed directions denoted by the arrows. If all signed flow values sum to zero (that is, inflow equals outflow) then the compartmental volume is constant.

Typically, the volume of perivascular fluid will change due to resistive axial flows during time increment, dt . If the combined Poiseuille resistance to flow from the west is denoted R_{west} and the combined Poiseuille resistance to flow from the east is denoted R_{east} , and if corresponding compartmental pressures are denoted P, then the incremental volume,

$$dV_{west} = i_{west}dt = \frac{P_{west}-P}{R_{west}}dt \ , \qquad (5)$$

and similarly,

$$dV_{east} = i_{east}dt = -\frac{P_east-P}{R_{east}}dt \ . \qquad (6)$$

In addition, the expanding artery acts like a piston to push extra volume, dV_{south} , radially upward into the perivascular space in short time increment, dt. Because the stiffness of artery wall is much greater than the stiffness of brain tissue, it is reasonable to regard the pulsating artery as a piston-like "volume source". Inner compression of the perivascular space by the arterial piston is given in terms of the local vascular compliance, C_{art} , and the local change in arterial pressure, dP_{art} . Using the derivative of the arterial pressure function,

$$dV_{south} = C_{art} \frac{dP_{art}(t)}{dt} dt \quad . \tag{7}$$

This volume is pushed into the segmental perivascular space, and creates an effective flow,

$$i_{south} = \frac{dV_{south}}{dt} . \tag{8}$$

Similarly, the expansion of multiple arteries in surrounding brain tissue will cause the brain surrounding the perivascular space to simultaneously expand like a piston to push extra volume, dV_{north} , radially downward in time dt, compressing the perivascular space from the north. However, simple calculations (not shown) suggest this effect is very small, compared to others, so that for purposes of the present model

$$i_{north} = dV_{north} = 0 . \tag{9}$$

Both dV_{south} and dV_{north} are counterbalanced by reactive elastic expansion or contraction of the underlying artery or the overlying brain tissue, caused by the resulting changes in the perivascular pressure. The reactive change in volume of the blood vessel, according to its compliance on the south side, is given by $C_{art} dP_{pvs}$. The reactive change in volume of the brain caused by compression on the north side, according to its compliance, is given by $C_{brain} dP_{pvs}$. The combined elastic effects produce a net change in perivascular pressure,

$$dP_{pvs} = \frac{dV_{pvs}}{C_{brain}+C_{art}} , \tag{10}$$

for total change in perivascular space volume, dV_{pvs} , or

$$dP_{pvs} = \frac{(dV_{west}+dV_{east}+dV_{south}+dV_{north}-C_{art}dP_{pvs}-C_{brain}dP_{pvs})}{C_{brain}+C_{art}} . \tag{11}$$

Solving for incremental perivascular pressure, dP_{pvs} ,

$$dP_{pvs}\left(1+\frac{C_{art}}{C_{brain}+C_{art}}+\frac{C_{brain}}{C_{brain}+C_{art}}\right) = \frac{(dV_{west}+dV_{east}+dV_{south}+dV_{north})}{C_{brain}+C_{art}} , \tag{12}$$

and

$$dP_{pvs} = \frac{dV_{west}+dV_{east}+dV_{south}+dV_{north}}{2(C_{brain}+C_{art})} . \tag{13}$$

In this dynamic system incremental volumes, dV_{east} , dV_{west} , dV_{south} , and dV_{north} , change with every time step, dt . Compartmental volumes, V_{art} and V_{pvs} , continually change as functions of time, and must be re-computed after each time step, dt , as $V_{art} = V_{art} + dV_{art}$ and $V_{pvs} = V_{pvs} + dV_{pvs}$.

Now, knowing the incremental change in perivascular pressure, dV_{pvs} , one can calculate the net change in perivascular compartment volume,

$$dV_{pvs} = dV_{west} + dV_{east} + dV_{south} + dV_{north} - C_{art}dP_{pvs} - C_{brain}dP_{pvs} . \quad (14)$$

Thus every time step, dt , one can update compartmental volumes as

$$V_{art} = V_{art} + dV_{south} - C_{art}dP_{pvs} , \quad (15)$$

and

$$V_{pvs} = V_{pvs} + dV_{pvs} . \quad (16)$$

Then, for cylindrical sectors spanning angle $\Delta\theta$, such as $\pi/2$ radians, and noting that $V_{art} = \left(\frac{\Delta\theta}{2\pi}\right)\pi r_1^2 L$ and $V_{art} + V_{pvs} = \left(\frac{\Delta\theta}{2\pi}\right)\pi r_2^2 L$, one can also update values of radii

$$r_1 = \sqrt{\frac{2V_{art}}{\Delta\theta L}} \quad (17)$$

and

$$r_2 = \sqrt{\frac{2(V_{art}+V_{pvs})}{\Delta\theta L}} . \quad (18)$$

The forgoing treatment allows computation of changes in perivascular pressures, volumes, and radii, for trees of brain penetrating arteries and periarterial spaces. For companion veins, similar expressions apply, with suitable subscript changes to denote veins, rather than arteries, namely V_{vein} , C_{vein} and with r_1 and r_2 being specific for veins rather than arteries.

The upgraded values of artery and cuff radii allow for subsequent re-calculation after every time increment, dt , of axial resistance to flow of CSF along the axis of the perivascular space in the model, as described in detail subsequently.

Compliance of vascular segments

Values for model compliances (change in volume divided by change in pressure, or $\Delta V/\Delta P$) can be estimated from vascular ultrasound and from textbook anatomy and physiology. For a sector $\Delta\theta$ of an elastic tube or blood vessel of length, L, and radius, r , that expands by amount, Δr , in response to transmural pressure change, ΔP . The compliance

$$C = \frac{\Delta\theta r L \Delta r}{\Delta P} = \frac{\Delta\theta r^2 L}{\Delta P}\left(\frac{\Delta r}{r}\right). \quad (19)$$

For a quarter cylinder domain as shown in Figure 6

$$C = \frac{\pi r^2 L}{2\Delta P}\left(\frac{\Delta r}{r}\right). \quad (20)$$

Here, in computing compliances, values of $\Delta P(n)$ for venules at branching level, n , in a tree of N total branching levels, are 1 mmHg*(1 – n/N), and values of ΔP for arteries are 20 mmHg*(1 – n/N), in keeping with the linear change in pressure down branching vascular trees.

Domain compliance for brain tissue of constant stiffness

As shown in Appendix 2, it is easy to demonstrate from basic mechanical principles that the compliance, C , of a sector, $\Delta\theta$, of a cylindrical segment of brain tissue in Figure 7 is given by the expression

$$C = \frac{\Delta\theta r_2^2 L}{E} ln\left(\frac{r_3}{r_2}\right), \quad (21)$$

where E represents Young's modulus of stiffness for brain tissue[21], and ln() represents the natural logarithm.

Resistance of segmental perivascular spaces to axial fluid flow

To calculate resistance, imagine the perivascular space as being split longitudinally and opened to form a flat sheet with a width equal to the average radius, $\Delta\theta(r_1+r_2)/2$, and a thickness of $r_2 - r_1$. Classically[12], for flow of a fluid having viscosity, μ , between two parallel plates of width $\Delta\theta(r_1+r_2)/2$, length L, and separation $r_2 - r_1$, we have axial resistance of the perivascular space

$$R_{pvs} \approx \frac{12\mu L}{\Delta\theta\frac{(r_1+r_2)}{2}(r_2-r_1)^3} = \frac{24\mu L}{\Delta\theta(r_2+r_1)(r_2-r_1)^3}, \quad (22)$$

or for $\frac{r_1}{r_2} = \lambda$,

$$R_{pvs} \approx \frac{24\mu L}{\Delta\theta\, r_2^4\, (1+\lambda)(1-\lambda)^3}\,. \tag{23}$$

This is a reasonable approximation to the resistance to axial flow in the cuff of fluid forming the perivascular space. To include instantaneous changes in this nonlinear resistance, R , it is necessary to account for small, time-varying changes in the arterial and perivascular radii, which must be recomputed each time step, dt .

Then, to calculate axial resistance between perivascular cuffs of different branches, one can compute interface resistance as series combination of upstream and downstream half segments

$$R_{east}(n) \approx \frac{1}{2}(R_n + R_{n+1}) \tag{24}$$

and

$$R_{west}(n) \approx \frac{1}{2}(R_{n-1} + R_n)\,. \tag{25}$$

Hydraulic resistance of tissue domains

As shown in Appendix 3, it is possible using Darcy's Law, to compute an analytical expression for the resistance to radial flow between paired periarterial and perivenous sectors, $\Delta\theta$. For two back-to-back overlapping sectors of cylindrical domains of inner radius r_2, outer radius r_3, and lengths, L , having hydraulic permeability constant, κ , the hydraulic resistance to flow of fluid with viscosity, μ , is given by the expression

$$R_{brain} = \frac{2\mu}{\kappa L \Delta\theta}\, ln\left(\frac{1}{4}\frac{r_3^2}{r_2^{art}.r_2^{vein}}\right), \tag{26}$$

where superscripts art and vein denote the perivascular radii.

Washout times of tissue domains

The washout time for the paired arterial and venous domains would be given by total interstitial fluid volume (ISF in ml) divided by volumetric interstitial fluid flow (in ml/sec) or

$$t_{washout} = \frac{tissue\ volume * ISF\ volume\ fraction}{\frac{arteriovenous\ perivascular\ pressure\ difference}{hydraulic\ resistance}}\,. \tag{27}$$

The volume of interstitial fluid between periarterial and perivenous spaces in the diamond shaped columns in Figures 5 and 6 is

$$V_{ISF} = 2\sigma_{ISF}\,\pi\left(\frac{r_3}{2}\right)^2 L\,\frac{\Delta\theta}{2\pi} = \frac{1}{4}\sigma_{ISF}\, r_3^2 L\Delta\theta\,. \tag{28}$$

The interstitial fluid flow is the arteriovenous difference in time averaged perivascular pressure, ΔP_{pvs} , divided by the local hydraulic resistance, R_{brain} , or

$$flow = \frac{\Delta P_{pvs}}{\frac{2\mu}{\kappa L \Delta\theta} ln\left(\frac{1}{4}\frac{r_3^2}{r_2^{art}.r_2^{vein}}\right)} . \quad (29)$$

The washout time for the interstitial fluid is

$$t_{washout} = \frac{V_{ISF}}{flow} = \frac{\frac{1}{4}\sigma_{ISF}\, r_3^2 L \Delta\theta}{\frac{\Delta P_{pvs}}{\frac{2\mu}{\kappa L \Delta\theta} ln\left(\frac{1}{4}\frac{r_3^2}{r_2^{art}.r_2^{vein}}\right)}} = \frac{1}{2}\frac{\sigma_{ISF}\, r_3^2 \frac{\mu}{\kappa} ln\left(\frac{1}{4}\frac{r_3^2}{r_2^{art}.r_2^{vein}}\right)}{\Delta P_{pvs}} . \quad (30)$$

Smaller domains at higher branching levels, also having relatively smaller values of r_3/r_2, have shorter washout times. Hence the domains around smaller branch arteries and veins in brain tissue that are still surrounded by perivascular spaces are the focus of glymphatic flow.

Numerical values of model parameters

Table 1 presents specific numerical values of input parameters of the standard normal model.

Table 1. Standard Model Parameters

Symbol	Definition	Value	Units
α	Vascular size reduction at each branching level	0.75	
β	Radial tissue size reduction at each branching level	0.888	
PVratio	Perivascular space to vessel ratio (r_2/r_1)	2	
dt	Time increment for numerical integration	0.0001	sec
ε_{art}	Fractional expansion of artery diameter with pulse	0.1	
ε_{vein}	Fractional expansion of vein diameter with pulse	0.03	
Freq	Cardiac frequency or pulse rate	1	Hz
κ	Darcy's Law hydraulic permeability of brain tissue	1.2×10^{-11}	cm^2
L(1)	Length of first vascular segment at the brain surface	1	cm
μ	Viscosity of cerebrospinal fluid	0.01	$dyne/cm^2$-sec
E_{brain}	Young's modulus of brain tissue	10000	$dyne/cm^2$
N	Number of branching levels in vascular tree	10	
π	Circle ratio	3.1416	
ΔP_{max}^{art}	One half pulse pressure in brain surface artery	20	mmHg
ΔP_{max}^{vein}	One half pulse pressure in brain surface vein	1	mmHg
ΔP_{max}^{sas}	One half pulse pressure in subarachnoid space CSF	2	mmHg
$r_1(1)$	Radius of first parent brain artery	0.03	cm
r3_r2	Ratio of domain radius to PVS radius at any level	12	
σ_{ISF}	Interstitial fluid volume fraction	0.15	

Vascular dimensions are based upon classical anatomy[22]. Pulsatile arterial and venous expansion fractions are based on those observed clinically for retinal arteries and veins through an ophthalmoscope. Venous to arterial diameter ratios are based on light microscopic images. Extracellular fluid volume fraction in brain is 18% to 20% in the cerebral cortex in several species[23]. However, since interstitial fluid volume equals extracellular fluid minus intravascular fluid; the interstitial fluid volume fraction is estimated at 15%. A consensus value is chosen for Young's elastic modulus, E , of brain tissue[21]. Multiple sources give values for the amplitude of pulsatile changes in intracranial pressure [16,24-26]. The hydraulic permeability of brain is from the recent studies and Vidotto[27] and Vidotto's tabulated summary of published values.

Numerical methods

Code is written in Microsoft Visual Basic and executed on an ordinary laptop computer. Pressures, volumes, axial resistances for a particular vascular domain, either arterial or venous, are computed iteratively for successive small time steps, dt = 0.0001 sec, from "cold start" initial conditions (mean ICP in all compartments) until the pulsatile pressure changes and the time averaged pressure differences become stable, reaching a steady-state. Pulsatile changes in arterial pressure and similar pulsatile changes from mean ICP are computed using approximate arterial pulse waveforms

$$\Delta P(t) = \Delta P_{max}\left[(\sin(\omega t) + \tfrac{1}{2}(\sin(2\omega t))\right]. \qquad (31)$$

For intracranial pressure pulses in the subarachnoid space $\Delta P_{max} = \Delta P_{max}^{sas}$ (2 mmHg in the standard model). For arterial pulses in branched segment of order, n , the pulse amplitude diminishes linearly as $P_{max}(n) = \Delta P_{max}^{art}\left(1 - \frac{n-1}{N}\right)$. For internal venous pressure a simple sinusoidal function having a phase shift of π radians and an amplitude of 1 mmHg is substituted for Equation (31). The standard simulation duration is 30 seconds, after which pressures and volumes become stable. In real time each arterial or venous pressure simulation requires less than 10 seconds to execute. The core algorithm for numerical integration of model variables can be outlined as follows:

COMPUTATIONAL ALGORITHM

```
Initialize variables

Compute time varying ΔICP using an approximate arterial pulse waveform

For each time step, dt {

    Compute instantaneous minus mean subarachnoid space pressure

    For each segment, n , compute {
      dVwest [Eq. 5]
      dVeast [Eq. 6]
      incremental arterial or venous pressure [Eq. 31]
      dVnorth [Eq. 9]
      dVsouth [Eq. 8]
      dPpvs [Eq. 13]
      Ppvs(n) = Ppvs(n) + dPpvs
      dVpvs = dVwest + dVeast + dVsouth + dVnorth – Cart(n) * dPpvs – Cbrain(n) * dPpvs [Eq. 14]
      Vpvs(n) = Vpvs(n) + dVpvs
      r1(n) [Eq. 17]
      r2(n) [Eq. 18]
      Rpvs(n) [Eq. 23]
    }

}
```

Typical outputs include perivascular pressures, volumes, and radii. Washout times for interstitial fluid compartment of brain tissue in hours are calculated using Eq. (30) and Eq. (4).

Results

Time domain waveforms of arterial and intracranial pressures

Figure 8 shows the time domain pressure waveforms in peri-arterial and peri-venous spaces of a middle level branch (n = 5 of 10). The tracings show instantaneous cyclic changes in intra-arterial pressure and in intracranial pressure at steady state. In the standard model cerebrospinal fluid flows in and out of brain surface openings of the Virchow-Robin spaces in response to changes in ICP, causing cyclic changes in pressure. Peri-arterial pressure is boosted by relatively greater expansion of arteries during cardiac systole.

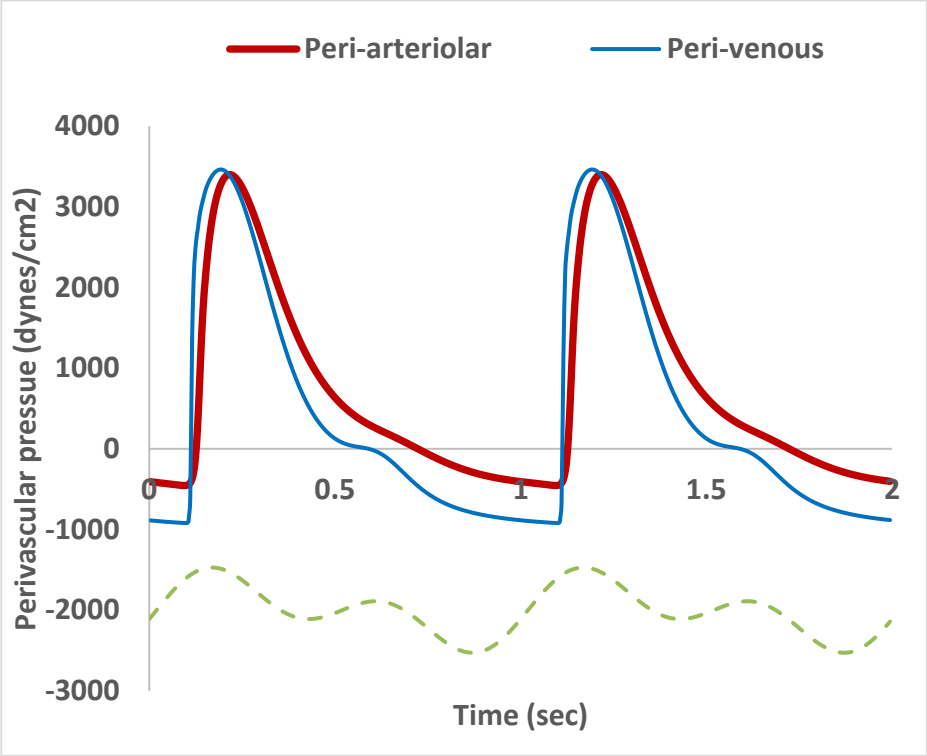

Figure 8: Pressure tracings for a middle branch at level 5 after 30 sec of steady pumping. Dashed curve represents scaled arterial pulse waveform as a timing reference.

Figure 9 illustrates time domain waveforms of vascular and perivascular radii in middle level (n = 5) arterial and venous branches. Radii r_1 represent the blood vessel and radii r_2 represent the CSF filled perivascular space.

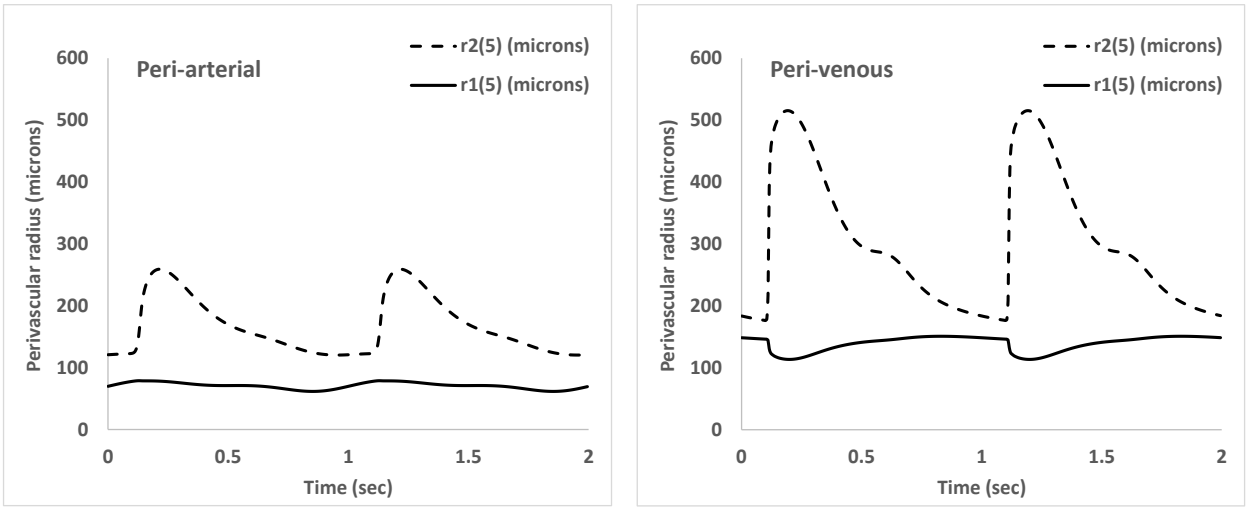

(a) (b)

Figure 9: Time domain waveforms of perivascular (r_2) and vascular (r_1) radii at branching level 5, illustrating pumping mechanism. Venous and perivenous radii are larger than arterial and periarterial radii according to normal anatomy. (a) on the arterial side, both artery walls and Virchow-Robin spaces expand during systole and taper during diastole. (b) on the venous side, vein walls collapse partially during systole. Perivascular space width, $r_3 - r_2$, is smaller around arteries than around veins.

The arterial radii (a) are less than the venous radii (b), as expected from normal anatomy. On the arterial side, radius, r_1 (solid curve) expands slightly, as expected about 5 percent during systole. Volume of the periarterial space increases due to inflow from the subarachnoid space. The outer wall of the perivascular space having radius r_2 (dashed curve) expands according of the compliance of the channel through soft brain tissue. In contrast, on the venous side, the softer wall of the larger diameter vein, which is distended by much lower blood pressure, collapses in response to inflow from the subarachnoid space. The outer wall of the surrounding perivenous space expands according to the compliance of the larger venous channel through soft brain tissue. There is a relatively greater net expansion of the perivenous space in response to fluid inflow from the subarachnoid space. On the arterial side, the narrowed channel seems to slow outflow back into the subarachnoid space between pulses more than on the venous side, allowing the time-averaged perivascular pressure difference to persist.

Time averaged perivascular pressure gradients

Figure 10 shows the difference between mean pressure inside the perivascular spaces surrounding arteries and mean pressure inside the perivascular spaces surrounding veins, plotted as a function of the radius of the artery. The differences are greater in the smaller diameter perivascular spaces surrounding more distal vascular branches. These spaces have arteries less than 50 microns in radius or less than 100 microns in diameter.

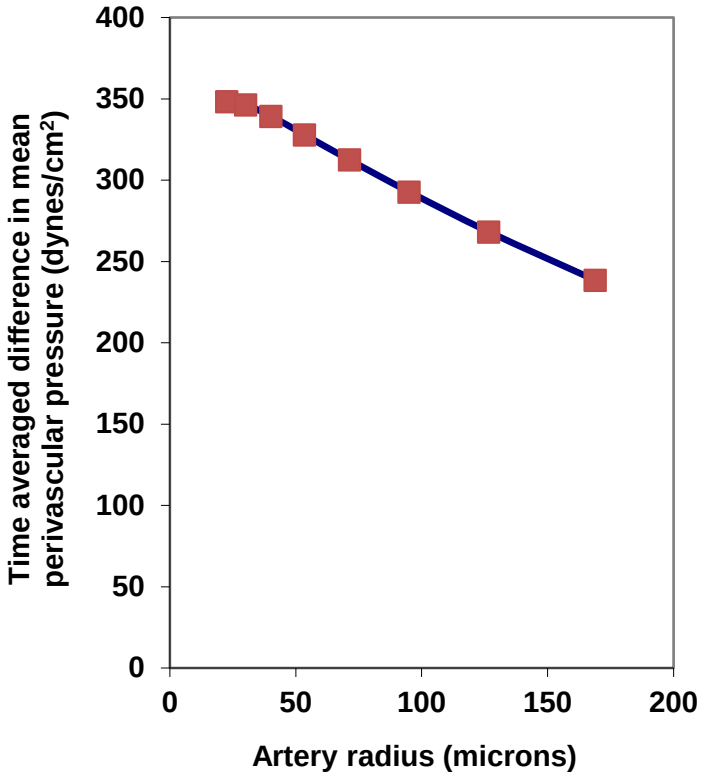

Figure 10: Time averaged pressure differences in dynes/cm^2 between neighboring periarterial and perivenous spaces as a function of local artery radius.

Figure 11 shows steady-state perivascular arteriovenous, or AV, pressure differences at branching level 5 as a function of relative perivascular space width, quantified as the cuff ratio. The cuff ratio is defined as the radius of the perivascular space divided by the radius of the local artery or vein. A cuff ratio of 1.00 would indicate a zero-width perivascular space. In the standard normal model, the cuff ratio is 2.0. The generation of a positive AV perivascular difference is dependent on a relatively narrow perivascular space width and a relatively small cuff ratio.

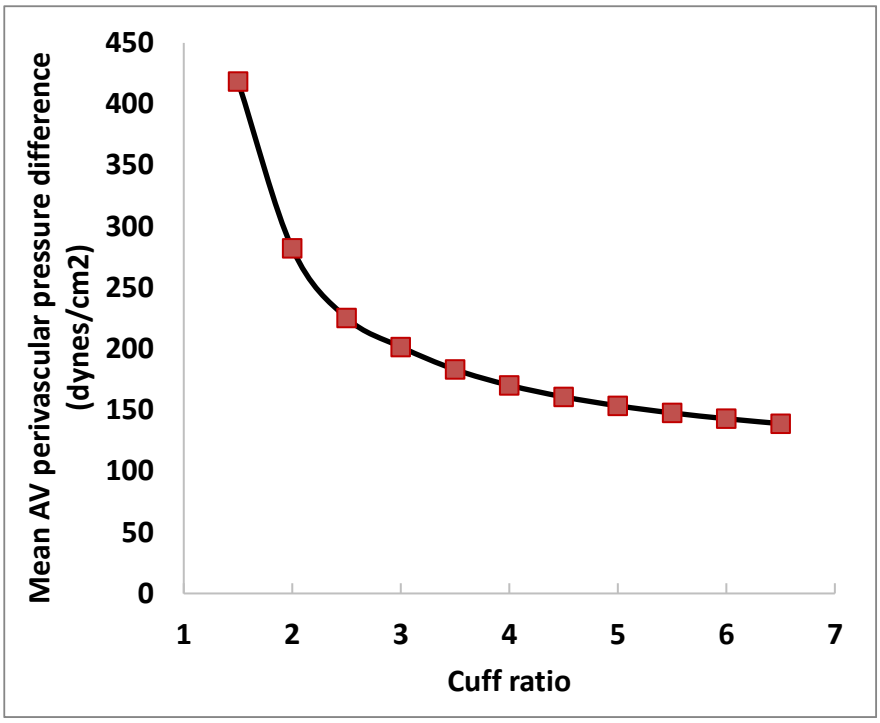

Figure 11: Mean periarterial minus perivenous pressures as a function of the cuff ratio, defined as the radius of the perivascular space to the radius of the local artery or vein. A cuff ratio of 1.00 would indicate a zero-width perivascular space. A cuff ratio of 2 is roughly normal. AV denotes arteriovenous.

Washout times

Figure 12 shows the calculated washout times (Eq. 30) for interstitial spaces in cylindrical tissue domains at various branching levels and corresponding arterial radii. Note the log scale of washout time on the vertical axis. The data points represent branching levels 3 through 10. Biologically meaningful bulk flow of interstitial fluid through brain tissue in response to perivascular pumping of cerebrospinal fluid occurs only in smaller branches of the arterial and venous vascular trees. Only the higher branching levels with the smaller vascular diameters have washout times less than 10 hours. A middle value for these branches is about 6 hours.

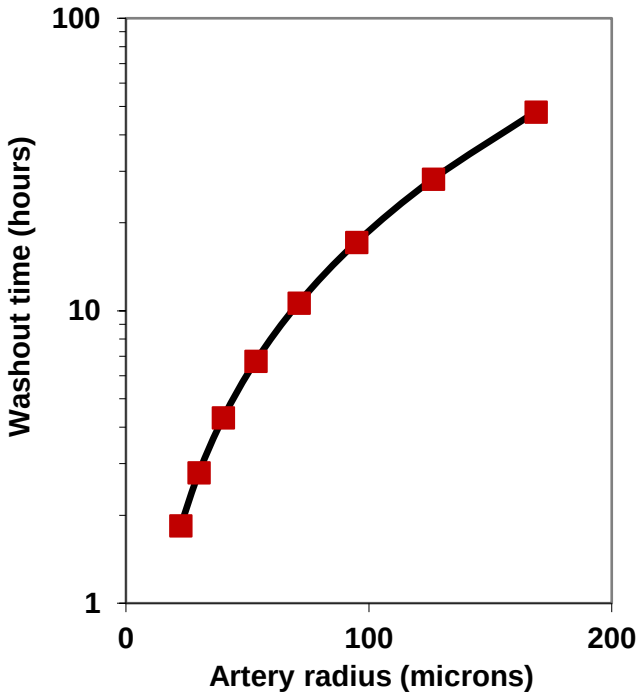

Figure 12: Calculated interstitial space washout times from simulated glymphatic flow as a function of penetrating artery size and branching level. Note vertical log scale.

Discussion

When the branching structure of vascular trees is properly considered, the classical anatomy of the Virchow-Robins space hides a surprising pump mechanism. Bringing together biomechanics, fluid mechanics, anatomy, and physiology, one can show in detail how glymphatic flow could occur, driven by a net time averaged positive pressure difference between distal branches of periarteriolar and perivenular Virchow-Robin spaces. Perivascular pumps work better at smaller scales. At the level of medium to small scale vessels, the flow is sufficient to cause a complete washout or replacement of interstitial fluid between brain cells every 1 to 10 hours.

Intriguingly, the human choroid plexus secretes ~1 L of CSF per day[28], which is similar to the rate of glymphatic flow calculated here. For example, choroid plexus secretion of 1000 ml/24hours = 41.7 ml/hour, which for a 1500-gram brain, having an interstitial fluid volume of about 0.15*1500 ml = 225 ml, would correspond to a turnover time of 225/41.7 = 5.3 hours. This value is in the middle range of the predicted turnover times in Figure 12 for the three highest levels of branching with artery radii in the range of 25 to 50 microns, or 50 to 100 microns in diameter. This observation suggests that the full volume of freshly secreted cerebrospinal fluid might seep through whole brain tissue by glymphatic flow. Perhaps macroscopic production and distribution of CSF over the brain surface, together with microscopic glymphatic pumping, constitute a unitary and integrated system for tissue waste removal.

The present mechanism has biological significance both for normal physiology and pathophysiology. CSF flow is now known to be increased during sleep[29]. During sleep higher pulse pressure from slower heart rates, and superimposed swings in ICP associated with slower breathing may boost the effectiveness of the present pump mechanism. Greater clearance of waste products and toxins may explain the refreshing effects of sleep, as well as of strenuous exercise, in which increased arterial pulsation and increased respiratory swings in blood pressure occur. Further, the proposed mechanism offers an unappreciated reason why cerebral arteries have thinner walls than systemic arteries of similar caliber: they pulsate more and drive the perivascular pump better.

There are also links to several important disease states[1,3,8]. Clearance of amyloid beta, a putative toxin causing Alzheimer's disease, may be reduced by impaired glymphatic flow[8,30-32]. Cerebral atherosclerosis may reduce distal arteriolar pulsations and impair glymphatic flow, leading to accelerated vascular dementia or by a glymphatic related mechanism as well as an ischemic one. Similarly in ischemic strokes, reduced clearance of postischemic toxins, including reactive oxygen species, may further amplify ischemic tissue damage[33]. In hypertension raised blood pressure causes arterial stiffening owing to nonlinear compliance of blood vessels, which would also diminish arterial pumping[1,34]. Also, as demonstrated here, the enlarged perivascular spaces resulting from neuronal loss in vascular dementia and in Alzheimer's disease[8,35], would contribute to an acceleration of such pathologies, owing to reduced glymphatic flow[36].

In turn, there are potential implications of small branch perivascular pumping for diagnosis and treatment. Diagnostically, there may be useful information in the amplitude of retinal arterial and venous pulsations[37,38]. The cornea provides a practical window on the intracranial microvasculature. Retinal arterial pulsations might be used as a noninvasive screening test. Therapeutically, arteriolar volumetric pumping might be increased by vasodilator drugs, which could increase washout of beta amyloid in early cases of Alzheimer's disease. Beta blockers, which can increase systemic pulse pressure generated by nonischemic hearts, as well as exercise, could promote better glymphatic waste removal.

Predictions of the present model are supported by experimental evidence. For example, Rosenberg et al.[39] used the radiotracer paradigm to look for bulk flow in the extracellular space of the cat caudate nucleus. They concluded that there was flow in white matter bundles with a velocity of 10.5 microns/min. These results are in agreement with the present model predictions. A migration speed of 10 microns/min = 10*60*24 microns/day = 14400 microns/day = 1.4 cm/day. For 6^{th} order brain domains located about 0.14 cm apart, it would take 0.14 cm /1.4 (cm/day) = 0.1 days, or 2.4 hours for washout. This finding is in reasonable agreement with predictions of the present model (Figure 12).

Others have described theoretical and numerical models of glymphatic flow[4]. Previously Hadaczek et al.[40] described a mechanism called ‘‘perivascular pumping”[34]. Ray et al.[13] showed that in vivo radioactive tracer measurements could be matched more accurately with a model that included advective transport with flow speeds of about 10 microns/min. Recently, Rey and Sarntinoranont[41] described a resistive flow network from intraarterial spaces, through brain tissue, to intravenous spaces with no net flow over time; however the perivascular spaces, axial perivascular flow, and axial perivascular resistance are not included. The present work shows that these features are critical.

Importantly, the present model does NOT simulate peristaltic pumping, associated with the travel and milking action of pulse waves along the perivascular spaces[42]. Typical segments of real perivascular networks are shorter than the arterial pulse wavelength by a factor of 1/10,000 or less (10 m/sec x 1 sec pulse period = 10 meters, compared to less than 0.001 meter in smaller branched tissue domains) making true peristaltic pumping unlikely. Kedarasetti[43] showed that peristaltic arterial pulsations can drive oscillatory flow of CSF but not directional pumping. However, in keeping with the present model and concept, Kazimierska et al.[44] suggested the importance of elasticity of the brain tissue surrounding perivascular spaces. They viewed the brain as a porous medium that is soft enough to be deformed appreciably by the pressures squeezing fluid through pores, and they concluded that further study of poroelastic pumping is warranted.

The present paper presents a new, first-principles mechanism for glymphatic fluid flow. Biologically meaningful amounts of flow could happen between smaller periarteriolar and perivenous spaces in human sized brains. Although full scale fluid dynamic simulations of multiple branched systems in three dimensions are computationally daunting and very time consuming; here geometric simplifications allow easy computation of the major branching effects. After accounting for the branching structure of vascular trees, the annular channels of the Virchow-Robin space, well known for over a century, provide a plausible pump mechanism that has been hiding in plain sight.

Appendix 1 details, justifying branch reduction factor of 0.75

It is helpful to specify resistance at each branching level to determine arterial pressure at each branching level: pressure drop = aggregate flow*aggregate local resistance at each level. For linear shortening factor β, for EACH individual segment, aggregate local resistance to blood flow in an arterial tree for all parallel branches at level n is

$$R_n \propto \left(\frac{\beta}{\beta^4}\right)\frac{1}{2^n}\,, \tag{A1}$$

and

$$\frac{R_n}{R_{n-1}} = \frac{\left(\frac{1}{\beta^3}\right)^n \frac{1}{2^n}}{\left(\frac{1}{\beta^3}\right)^{n-1} \frac{1}{2^{n-1}}} = \frac{1}{2\beta^3}\,. \tag{A2}$$

Case 1:

$$\text{If } \beta = \sqrt[3]{\frac{1}{2}} = 0.794, \text{ then } \frac{R_n}{R_{n-1}} = 1\,, \tag{A3}$$

there will be equal resistances and equal total pressure drops at each branch point in the model arterial tree.

Case 2:

On the other hand, for equal total cross-sectional area at each branch point we have $\beta = \frac{1}{\sqrt{2}} = 0.707$. In this case

$$\frac{R_n}{R_{n-1}} = \frac{1}{2\beta^3} = \frac{2\sqrt{2}}{2} = 1.414\,. \tag{A4}$$

The relative internal pressure drop across each branch level would be

$$\frac{\Delta Part_n}{\Delta Part_{n-1}} = \frac{R_n}{R_{n-1}}\frac{1}{2\beta^3} = 1.414\,. \tag{A5}$$

To approximately satisfy desirable both factors in an idealized model system, one might select

$$\beta = \frac{0.794+0.707}{2} = 0.75\ . \qquad \text{(A6)}$$

This is a branch reduction factor that is approximately ideal and allows roughly equal flow at all branch levels and also a linear decrease in internal arterial pressure.

Appendix 2: compliance of a brain domain

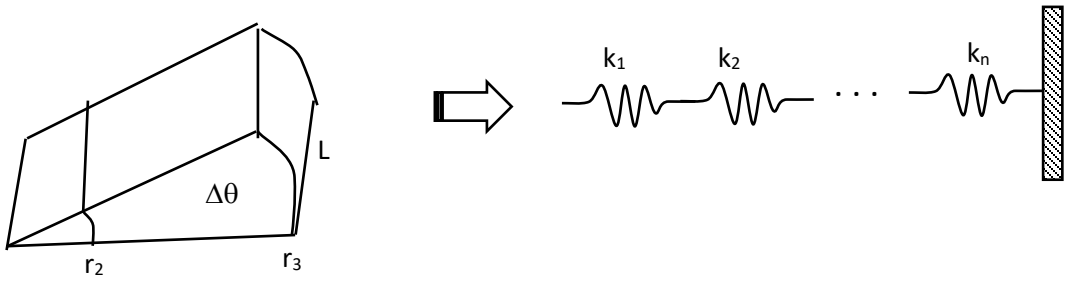

(a) (b)

Figure 13: Compression of wedge-shaped sector of an elastic cylinder.

Figure 13 (a) shows a wedge-shaped section of a cylindrical brain domain of angle $\Delta\theta$. Radius, r_2 , represents the outer border of the perivascular space. Ordinary brain tissue fills the wedge shape from r_2 to r_3 . To appreciate the elastic properties of this composite structure, consider multiple radial layers of brain, dr thick, as constituting series springs as shown in (b). The series springs are characterized by spring constants, k_1 , k_2 , and so on. Quantitatively, the reactive force produced by compression of the stacked springs in Figure 13 (b) by total amount, Δx is given by $F = k_{total}\,\Delta x$, where the combined spring constant, k_{total} , of the series springs is classically given by the expression

$$\frac{1}{k_{total}} = \frac{1}{k_1} + \frac{1}{k_2} + \cdots + \frac{1}{k_n}\ . \qquad \text{(A7)}$$

For a rectangular elastic solid of surface area A, thickness, h, and Young's modulus of stiffness, E , the effective spring constant is given by the formula, k = "EA/h". Young's modulus tissue is a known material property of brain tissue (~ 1 kPa). Hence, by calculus, we can write

$$\frac{1}{k_{total}} = \int_{r_2}^{r_3} \frac{dr}{ELr\Delta\theta} = \frac{1}{EL\Delta\theta}\int_{r_2}^{r_3} \frac{1}{r}\,dr = \frac{1}{EL\Delta\theta}\,ln\left(\frac{r_3}{r_2}\right)\ . \qquad \text{(A8)}$$

Inverting Equation A8, the lumped spring constant of the stacked layers of ordinary brain tissue in one cylindrical domain

$$k_{total} = \Delta\theta \frac{E_{brain}\, L}{\ln\left(\frac{r_3}{r_2}\right)} . \quad \text{(A9)}$$

The reactive pressure from expansion of the perivascular space of radius r_2 equals the reactive force divided by area, $k_{total} * \Delta r_2$ / surface area or

$$\Delta P = \frac{k_{total}\Delta r_2}{r_2 \Delta\theta L} = \Delta\theta \frac{E_{brain}\, L}{\ln\left(\frac{r_3}{r_2}\right)} \frac{\Delta r_2}{r_2 \Delta\theta L} = \frac{E_{brain}}{\ln\left(\frac{r_3}{r_2}\right)} \frac{\Delta r_2}{r_2} . \quad \text{(A10)}$$

The compliance of the sector of brain tissue is the incremental change in volume divided by the incremental change in pressure

$$C = \frac{\Delta V}{\Delta P} = \frac{r_2\, \Delta\theta L \Delta r_2}{\frac{E_{brain}\ \Delta r_2}{\ln\left(\frac{r_3}{r_2}\right)\ r_2}} = \frac{r_2^2\, \Delta\theta L}{E_{brain}} \ln\left(\frac{r_3}{r_2}\right) . \quad \text{(A11)}$$

Appendix 3: hydraulic resistance of the brain tissue domains

Applying Darcy's law for the flow of a viscous fluid through a porous medium, the fluid flow, $Q = \frac{\kappa A \Delta P}{\mu L}$, where ΔP is the pressure difference across the medium, L is the length in the direction of flow, A is the cross-sectional area perpendicular to flow, μ is the fluid viscosity, and κ is permeability constant of the medium, the hydraulic resistance to fluid flow through a rectangular solid permeable medium is

$$R = \frac{\Delta P}{Q} = \frac{\mu L}{\kappa A} . \quad \text{(A12)}$$

This expression can be used to find the series resistance of two overlapping quarter cylindrical domains providing a diamond shaped path from the periarterial space to the perivenous space as shown in Figures 5 and 6.

Consider the resistance of either periarterial or perivenous tissue domain having radius approximately equal to one half the distance between an artery and a vein at a given segmental level, namely $r_3/2$. Using an algebraic approach very similar to that in Appendix 2 for concentric cylindrical shells, we have for a differential shell of brain tissue dr thick, at radius r , and having length, L , over sector Δθ ,

$$dR = \frac{\mu}{\kappa} \cdot \frac{dr}{r \Delta\theta L} . \quad \text{(A13)}$$

Integrating, the resistance for one arterial or venous sector from r_2 to $\frac{r_3}{2}$ is

$$R_1 = \int_{r_2}^{\frac{r_3}{2}} \frac{\mu dr}{\kappa L r \Delta\theta} = \frac{\mu}{\kappa L \Delta\theta} \int_{r_2}^{\frac{r_3}{2}} \frac{1}{r} dr = \frac{\mu}{\kappa L \Delta\theta} ln\left(\frac{1}{2}\frac{r_3}{r_2}\right) \quad \text{(A14)}$$

in terms of known material tissue properties and geometry. Note, however, that the perivascular radius, r_2 , for veins is not equal to, and typically larger than, the perivascular radius, r_2 , for arteries. During fluid flow from the periarterial space to the perivenous space, the back-to-back arterial and venous domains are in series. Series resistances add. So, the total resistance to flow from artery to vein is

$$R_{brain} = \frac{\mu}{\kappa L \Delta\theta} ln\left(\frac{1}{2}\frac{r_3}{r_2^{art}}\right) + \frac{\mu}{\kappa L \Delta\theta} ln\left(\frac{1}{2}\frac{r_3}{r_2^{vein}}\right) = \frac{\mu}{\kappa L \Delta\theta} ln\left(\frac{1}{4}\cdot\frac{r_3^2}{r_2^{art}\cdot r_2^{vein}}\right). \quad \text{(A15)}$$

References

1. Iliff JJ, Wang M, Liao Y, Plogg BA, Peng W, et al. (2012) A paravascular pathway facilitates CSF flow through the brain parenchyma and the clearance of interstitial solutes, including amyloid beta. Sci Transl Med 4: 147ra111.
2. Kelley D, Thomas J (2023) Cerebrospinal Fluid Flow. Annual Review of Fluid Mechanics 55: 237-264.
3. Rasmussen MK, Mestre H, Nedergaard M (2018) The glymphatic pathway in neurological disorders. Lancet Neurol 17: 1016-1024.
4. Bohr T, Hjorth PG, Holst SC, Hrabetova S, Kiviniemi V, et al. (2022) The glymphatic system: Current understanding and modeling. iScience 25: 104987.
5. Benveniste H, Liu X, Koundal S, Sanggaard S, Lee H, et al. (2019) The Glymphatic System and Waste Clearance with Brain Aging: A Review. Gerontology 65: 106-119.
6. Brinker T, Stopa E, Morrison J, Klinge P (2014) A new look at cerebrospinal fluid circulation. Fluids Barriers CNS 11: 10.
7. Linninger AA, Tsakiris C, Zhu DC, Xenos M, Roycewicz P, et al. (2005) Pulsatile cerebrospinal fluid dynamics in the human brain. IEEE Trans Biomed Eng 52: 557-565.
8. Gouveia-Freitas K, Bastos-Leite AJ (2021) Perivascular spaces and brain waste clearance systems: relevance for neurodegenerative and cerebrovascular pathology. Neuroradiology 63: 1581-1597.
9. Jessen NA, Munk AS, Lundgaard I, Nedergaard M (2015) The Glymphatic System: A Beginner's Guide. Neurochem Res 40: 2583-2599.
10. Tarasoff-Conway JM, Carare RO, Osorio RS, Glodzik L, Butler T, et al. (2015) Clearance systems in the brain-implications for Alzheimer disease. Nat Rev Neurol 11: 457-470.
11. Thomas JH (2019) Fluid dynamics of cerebrospinal fluid flow in perivascular spaces. J R Soc Interface 16: 20190572.
12. Christov IC (2021) Soft hydraulics: from Newtonian to complex fluid flows through compliant conduits. J Phys Condens Matter 34.
13. Ray L, Iliff JJ, Heys JJ (2019) Analysis of convective and diffusive transport in the brain interstitium. Fluids Barriers CNS 16: 6.
14. Schreder HE, Liu J, Kelley DH, Thomas JH, Boster KAS (2022) A hydraulic resistance model for interstitial fluid flow in the brain. J R Soc Interface 19: 20210812.
15. Wardlaw JM, Benveniste H, Nedergaard M, Zlokovic BV, Mestre H, et al. (2020) Perivascular spaces in the brain: anatomy, physiology and pathology. Nat Rev Neurol 16: 137-153.
16. Evensen KB, Eide PK (2020) Measuring intracranial pressure by invasive, less invasive or non-invasive means: limitations and avenues for improvement. Fluids Barriers CNS 17: 34.
17. Zweifach BW (1974) Quantitative studies of microcirculatory structure and function. II. Direct measurement of capillary pressure in splanchnic mesenteric vessels. Circ Res 34: 858-866.

18. Zweifach BW (1974) Quantitative studies of microcirculatory structure and function. I. Analysis of pressure distribution in the terminal vascular bed in cat mesentery. Circ Res 34: 843-857.
19. Davis MJ, Ferrer PN, Gore RW (1986) Vascular anatomy and hydrostatic pressure profile in the hamster cheek pouch. Am J Physiol 250: H291-303.
20. Jin BJ, Smith AJ, Verkman AS (2016) Spatial model of convective solute transport in brain extracellular space does not support a "glymphatic" mechanism. J Gen Physiol 148: 489-501.
21. Chatelin S, Constantinesco A, Willinger R (2010) Fifty years of brain tissue mechanical testing: from in vitro to in vivo investigations. Biorheology 47: 255-276.
22. Zhang ET, Inman CB, Weller RO (1990) Interrelationships of the pia mater and the perivascular (Virchow-Robin) spaces in the human cerebrum. J Anat 170: 111-123.
23. Levin VA, Fenstermacher JD, Patlak CS (1970) Sucrose and inulin space measurements of cerebral cortex in four mammalian species. Am J Physiol 219: 1528-1533.
24. Czosnyka M, Pickard JD (2004) Monitoring and interpretation of intracranial pressure. J Neurol Neurosurg Psychiatry 75: 813-821.
25. Eide PK, Holm S, Sorteberg W (2012) Simultaneous monitoring of static and dynamic intracranial pressure parameters from two separate sensors in patients with cerebral bleeds: comparison of findings. Biomed Eng Online 11: 66.
26. Holm S, Eide PK (2008) The frequency domain versus time domain methods for processing of intracranial pressure (ICP) signals. Med Eng Phys 30: 164-170.
27. Vidotto M, Bernardini A, Trovatelli M, De Momi E, Dini D (2021) On the microstructural origin of brain white matter hydraulic permeability. Proc Natl Acad Sci U S A 118.
28. Damkier HH, Brown PD, Praetorius J (2013) Cerebrospinal fluid secretion by the choroid plexus. Physiol Rev 93: 1847-1892.
29. Vijayakrishnan Nair V, Kish BR, Inglis B, Yang HS, Wright AM, et al. (2022) Human CSF movement influenced by vascular low frequency oscillations and respiration. Front Physiol 13: 940140.
30. Govindpani K, McNamara LG, Smith NR, Vinnakota C, Waldvogel HJ, et al. (2019) Vascular Dysfunction in Alzheimer's Disease: A Prelude to the Pathological Process or a Consequence of It? J Clin Med 8.
31. Carare RO, Bernardes-Silva M, Newman TA, Page AM, Nicoll JA, et al. (2008) Solutes, but not cells, drain from the brain parenchyma along basement membranes of capillaries and arteries: significance for cerebral amyloid angiopathy and neuroimmunology. Neuropathol Appl Neurobiol 34: 131-144.
32. Weller RO, Subash M, Preston SD, Mazanti I, Carare RO (2008) Perivascular drainage of amyloid-beta peptides from the brain and its failure in cerebral amyloid angiopathy and Alzheimer's disease. Brain Pathol 18: 253-266.
33. Shi J, Tang R, Zhou Y, Xian J, Zuo C, et al. (2020) Attenuation of White Matter Damage Following Deferoxamine Treatment in Rats After Spinal Cord Injury. World Neurosurg 137: e9-e17.
34. Mestre H, Tithof J, Du T, Song W, Peng W, et al. (2018) Flow of cerebrospinal fluid is driven by arterial pulsations and is reduced in hypertension. Nat Commun 9: 4878.
35. Double KL, Halliday GM, Kril JJ, Harasty JA, Cullen K, et al. (1996) Topography of brain atrophy during normal aging and Alzheimer's disease. Neurobiol Aging 17: 513-521.
36. Yamazaki Y, Kanekiyo T (2017) Blood-Brain Barrier Dysfunction and the Pathogenesis of Alzheimer's Disease. Int J Mol Sci 18.
37. Labounkova I, Labounek R, Kolar R, Tornow RP, Babbs CF, et al. (2022) Heart rate and age modulate retinal pulsatile patterns. Commun Biol 5: 582.
38. Ballerini L, McGrory S, Valdes Hernandez MDC, Lovreglio R, Pellegrini E, et al. (2020) Quantitative measurements of enlarged perivascular spaces in the brain are associated with

retinal microvascular parameters in older community-dwelling subjects. Cereb Circ Cogn Behav 1: 100002.
39. Rosenberg GA, Kyner WT, Estrada E (1980) Bulk flow of brain interstitial fluid under normal and hyperosmolar conditions. Am J Physiol 238: F42-49.
40. Hadaczek P, Yamashita Y, Mirek H, Tamas L, Bohn MC, et al. (2006) The "perivascular pump" driven by arterial pulsation is a powerful mechanism for the distribution of therapeutic molecules within the brain. Mol Ther 14: 69-78.
41. Rey J, Sarntinoranont M (2018) Pulsatile flow drivers in brain parenchyma and perivascular spaces: a resistance network model study. Fluids Barriers CNS 15: 20.
42. Wang P, Olbricht WL (2011) Fluid mechanics in the perivascular space. J Theor Biol 274: 52-57.
43. Kedarasetti RT, Drew PJ, Costanzo F (2020) Arterial pulsations drive oscillatory flow of CSF but not directional pumping. Sci Rep 10: 10102.
44. Kazimierska A, Kasprowicz M, Czosnyka M, Placek MM, Baledent O, et al. (2021) Compliance of the cerebrospinal space: comparison of three methods. Acta Neurochir (Wien) 163: 1979-1989.